Electric-field-driven exciton vortices in transition metal dichalcogenide monolayers

Yingda Chen [1,2] Yongwei Huang [1,2] Wenkai Lou [1,2,*] Yongyong Cai,[3,†] and Kai Chang[1,2,4,‡]

[1]*SKLSM, Institute of Semiconductors, Chinese Academy of Sciences, P.O. Box 912, Beijing 100083, People's Republic of China*
[2]*CAS Center for Excellence in Topological Quantum Computation, University of Chinese Academy of Sciences,*
Beijing 100190, People's Republic of China
[3]*Laboratory of Mathematics and Complex Systems (Ministry of Education), School of Mathematical Sciences,*
Beijing Normal University, Beijing 100875, People's Republic of China
[4]*Beijing Academy of Quantum Information Sciences, Beijing 100193, People's Republic of China*

We predict electric-field-driven exciton vortices in transition metal dichalcogenide monolayers in the Bose-Einstein condensation regime. The Rashba spin-orbit coupling created by perpendicular electric fields couples the bright and dark excitons, behaves like an emerging SU(2) gauge field for excitons, and induces spatially asymmetric distribution of exciton density. We find the interplay between the dipole-dipole interaction among excitons and Rashba spin-orbit coupling leads to the phase transitions containing different vortices, from a single pair of vortices to numerous satellite vortices appearing at the edge of the sample. The exciton condensation at the K and K' valleys shows mirror-symmetric patterns composed of exciton vortices rotating oppositely, which are protected topologically by the winding numbers.

I. INTRODUCTION

The emerging layered two-dimensional (2D) transition metal dichalcogenides (TMDs), such as MX_2 ($M =$ Mo, W; $X =$ S, Se, Te, ...), display unique optical properties generating significant interests [1–3]. Since the Coulomb interaction can not be fully screened in the 2D materials [4,5], the TMDs monolayers (MLs) possess strong excitonic effect even at room temperature and are expected to be an ideal platform to explore exciton physics and devices [6–8]. These materials also exhibit strong light-matter interactions, due to the enhanced excitonic effect. Understanding and manipulating the excitons are key to potential applications of 2D TMDs for future optoelectronic devices [9–14].

Excitons can be viewed as bosons when the paired electrons and holes are tightly bounded by the Coulomb interactions, therefore may collapse into a phase coherent state known as Bose-Einstein condensation (BEC) at low temperatures, and detected by the photoluminescence spectra [15–19]. The lifetime and binding energy of excitons are crucial for observing exciton BEC experimentally in solids. Long exciton radiative lifetime allows the excitons to build up a quasiequilibrium before recombination. Excitons in the solids with an indirect band gap are supposed to have long lifetimes. The exciton lifetime could also be enhanced by the spatial separation of electrons and holes, which can be induced by the type II band alignment, as well as the external electric fields.

Compared with the bulk semiconductor systems, the unscreened Coulomb interaction in TMD MLs leads to huge binding energies of excitons ranging from 0.4 to 1.1 eV [20–23], which show a linear scaling behavior as a function of the band gap of 2D materials [22,24]. The huge binding energy leads to small Bohr radius of excitons in TMD MLs and high average exciton density, resulting in the considerably high critical temperature of exciton BEC.

Recently, the condensation and the superfluidity of excitons are reported experimentally in the TMD van der Waals heterostructures [25–27], where the electrons and holes are separated at different TMD MLs. The properties of these condensates have also been investigated theoretically [28] at high temperatures [29], in the presence of the unscreened dipolar interactions between excitons [30]. Although the exciton BECs in the TMDs have been studied both theoretically and experimentally, the 2D exciton vortices in these materials remain unexplored.

Potential traps are required for BECs in a strict 2D system [31]. A conventional way to create in-plane potential traps has been employed using the band-gap engineering, e.g., the quantum confined Stark effect [32] and interface fluctuations [33] in coupled quantum wells [15,33–35]. In 2D semiconductor systems, excitons can also be confined in potential traps created by lateral confinements, i.e., the edges of the nanoflakes.

In this work we consider a flake of TMD ML, e.g., WSe$_2$, sandwiched by electrode gates shown schematically in Fig. 1(a). The electric field created by the electrode gates enhances lifetimes of excitons, and meanwhile leads to the Rashba spin-orbit coupling (RSOC), inducing a mixing of bright and dark exciton states [36], and leading to the formation of exciton vortices. Compared with exciton BEC

*wklou@semi.ac.cn
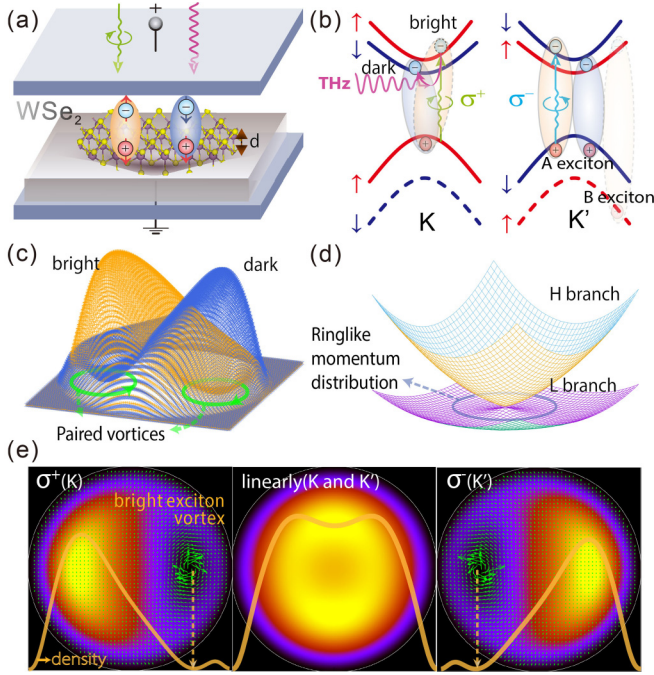†yongyong.cai@bnu.edu.cn
‡kchang@semi.ac.cn

FIG. 1. Bright and dark excitons in TMD MLs. (a) Excitons trapped in a circular flake ($R_0 = 0.3$ μm) of WSe$_2$ ML between the electrodes. (b) Optical transitions and the bright/dark A/B exciton states at the K and K' valleys. (c) Spatial separation of bright (left) and dark (right) excitons caused by RSOC, where a pair of bright and dark exciton vortices is also observed. (d) Dispersion of excitons at the L state (down) and H state (up). (e) Valley-selective density (color map) and velocity distributions (green arrows) of bright excitons pumped with σ_+, σ_-, and linearly polarized laser, with fixed number of bright and dark excitons. The orange solid lines show the density profile along the x axis, while the dashed lines indicate the vortex cores. $|\lambda_{BR}| = 18$ meV Å and $n_{b,d} = 10^{10}$ cm^{-2} in (d) and (e).

in coupled quantum wells, the TMD MLs possess unique features such as valley-spin locking and intrinsic spin-orbit coupling, which makes it possible to excite excitons at K/K' valley with opposite spins via the right (σ_+) or left (σ_-) circularly polarized laser [see Fig. 1(b)]. We find the interplay between the valley-selective exciton BEC and RSOC can induce a variety of BEC patterns as well as paired bright and dark vortices, which have not been observed in earlier systems like semiconductor quantum wells.

Our paper is organized as follows. In Sec. II, we derive the exciton Hamiltonian in TMD MLs under perpendicular electric field, and the coupled Gross-Pitaevskii (GP) equations including the dipole-dipole interaction (DDI) between excitons. The SU(2) gauge field induced by the RSOC created by the electric field, and hence the formation mechanism of exciton vortices are also given. In Sec. III, we give the numerical results and discussion. First, we solve the coupled GP equations by using the imaginary-time-propagation method, to study the ground-state exciton vortices and the phase (characterized by the winding number) transitions between different vortex states varying with RSOC. Second, we discuss the impact of DDI and various impurities on the BEC patterns and vortices. Third, we estimate the critical temperature of BEC in the TMD MLs, and discuss the experimental realization of

exciton vortices in different TMD MLs. In Sec. IV, we give the summary.

II. THEORY AND MODEL

To describe the motions of excitons, we first derive the Hamiltonian of noninteracting excitons in TMD MLs under the perpendicular electric fields. The low-energy $k \cdot p$ Hamiltonians of TMD MLs at the K/K' point can be written as in the 4×4 matrix form $\mathcal{H}$ constructed from the spinful orbital basis (d_{z^2} for conduction bands and $d_{x^2-y^2} + d_{xy}$ for valence bands) [37],

$$\mathcal{H} = \begin{bmatrix} \tilde{H}_c & \tilde{H}_{cv} \\ \tilde{H}_{vc} & \tilde{H}_v \end{bmatrix}, \qquad (1)$$

where the 2×2 matrices $\tilde{H}_c = [\frac{\hbar^2 |\mathbf{k}|^2}{4m_0}(\alpha + \beta) + \frac{\Delta}{2}]\mathbb{I} + \lambda_c \tau s_z$ and $\tilde{H}_v = [\frac{\hbar^2 |\mathbf{k}|^2}{4m_0}(\alpha - \beta) - \frac{\Delta}{2}]\mathbb{I} + \lambda_v \tau s_z$ describe the lowest conduction band and the topmost valence band, while $\tilde{H}_{cv} = (\tilde{H}_{vc})^\dagger = [a_0 t_0 (\tau k_x - ik_y)]\mathbb{I} + \tilde{H}_R$ represent the coupling between them. Here $s_{x,y,z}$ are the Pauli matrices denoting electron spin, m_0 is the free-electron mass, α, β are dimensionless parameters, a_0 is the lattice constant, t_0 is the effective hopping constant, and Δ is the energy gap. $\lambda_{c(v)} \tau s_z$ indicates the intrinsic spin-orbit splitting in the conduction (valence) band, with valley index $\tau = \pm 1$. $\tilde{H}_R = \alpha_R(\tau s_y + is_x)$ is the RSOC induced by the perpendicular electric field, due to the breakdown of the σ_h symmetry [38]. α_R is the RSOC parameter depending on the electric fields.

The single-band Hamiltonian can be obtained by applying Löwdin's perturbation theory [39] in the wide-band-gap limit

$$H_c = \begin{bmatrix} \frac{\hbar^2 |\mathbf{k}|^2}{2m_{c,+}} + \tau \lambda_c + \frac{V_0}{2} & \lambda_{BR}^* \mathbf{k}_- \\ \lambda_{BR} \mathbf{k}_+ & \frac{\hbar^2 |\mathbf{k}|^2}{2m_{c,-}} - \tau \lambda_c + \frac{V_0}{2} \end{bmatrix}$$

$$H_v = \begin{bmatrix} \frac{\hbar^2 |\mathbf{k}|^2}{2m_{v,+}} + \tau \lambda_v - \frac{V_0}{2} & -\lambda_{BR}^* \mathbf{k}_- \\ -\lambda_{BR} \mathbf{k}_+ & \frac{\hbar^2 |\mathbf{k}|^2}{2m_{v,-}} - \tau \lambda_v - \frac{V_0}{2} \end{bmatrix}, \quad (2)$$

where $\mathbf{k}_\pm = k_x \pm ik_y$, the effective mass of the conduction band $m_c^{\tau s} = [(\alpha + \beta)/2m_0 + 2a_0^2 t_0^2/\Delta_{\tau s}']^{-1}$, and of the valence band $m_v^{\tau s} = -[(-\alpha + \beta)/2m_0 + 2a_0^2 t_0^2/\Delta_{\tau s}']^{-1}$. The band gap $\Delta_{\tau s}' = \Delta + (\lambda_c - \lambda_v)\tau s$ is valley and spin dependent, as shown in Fig. 1(b). C_3 symmetry at the K point gives rise to the RSOC Hamiltonian as $\tilde{H}_{BR}^\tau = \lambda_{BR}^i(k_x s_y - k_y s_x) + \lambda_{BR}^r(k_x s_x + k_y s_y)$ [40]. Here the complex RSOC parameter $\lambda_{BR} = \lambda_{BR}^r + i\lambda_{BR}^i$, and $|\lambda_{BR}| = 2\alpha_R a_0 t_0 / \Delta_{\tau s}'$. $V_0 = \Delta + 4\alpha_R^2(1 - \tau s)/\Delta_{\tau s}' \approx \Delta$, when $\alpha_R^2 \ll \Delta_{\tau s}'$.

Neglecting the valley coupling at low temperatures [41], the Hamiltonian of the intravalley excitons can be represented as $H_{ex}^\tau = H_e^\tau(\mathbf{k}_e) + H_h^\tau(\mathbf{k}_h) + V(\mathbf{r}_e - \mathbf{r}_h)$, where $V(\mathbf{r}_e - \mathbf{r}_h)$ is the Coulomb interaction between the electrons and holes. With $\mathbf{k}_e = \mathbf{k}_c$ ($\mathbf{k}_h = -\mathbf{k}_v$), the electron (hole) Hamiltonian $H_e^\tau = H_c$ ($H_h^\tau = -H_v$) can be given by Eq. (2). Excitons composed of holes at the upper (lower) branch of the spin-splitted valence bands are named as A (B) excitons. In the wide-band-gap limit, the RSOC between the conduction and valence bands can be safely neglected, therefore, $\tilde{H}_{BR}^\tau(\mathbf{k}_e)$ in H_e^τ acts like the RSOC between bright and dark excitons, while $\tilde{H}_{BR}^\tau(\mathbf{k}_h)$ in H_h^τ which behaves like the RSOC between A and B excitons. Since the Zeeman-type intrinsic spin-orbit

splitting in the valence band $|\lambda_v|$ is giant, separating A and B excitons about $0.1 \sim 0.2$ eV [3,42,43], $\tilde{H}_{BR}^\tau(\mathbf{k}_h)$ (several meVs [40]) can be neglected. Therefore, A and B excitons can be decoupled.

We focus on the lowest A exciton at the K valley in this paper [Fig. 1(b)]. The Hamiltonian for A excitons at the K point in basis of the bright (with exciton spin $S = 0$) and dark states ($S = -1$) can be expressed as the 2×2 matrix

$$H_{\text{ex},K} = \begin{pmatrix} H_{b0} & H_{BR}^* \\ H_{BR} & H_{d0} \end{pmatrix}, \qquad (3)$$

where the Hamiltonian of the bright excitons $H_{b0} = H_{k,b} + \Delta_b' + V(\mathbf{r}_e - \mathbf{r}_h)$, the dark excitons $H_{d0} = H_{k,d} + \Delta_d' + V(\mathbf{r}_e - \mathbf{r}_h)$. Here $\Delta_b' = \Delta + \lambda_c - \lambda_v$ and $\Delta_d' = \Delta - \lambda_c - \lambda_v$. The kinetic energy of bright (dark) excitons $H_{k,b} = \hbar^2 k_e^2/2m_{e1} + \hbar^2 k_h^2/2m_{h1}$ ($H_{k,d} = \hbar^2 k_e^2/2m_{e2} + \hbar^2 k_h^2/2m_{h1}$), where the masses $m_{e1} = m_c^+$, $m_{e2} = m_c^-$, $m_{h1} = -m_v^+$, and the RSOC between bright and dark excitons $H_{BR} = \lambda_{BR}\mathbf{k}_{e+}$.

Since the effective masses of two spin-split conduction band branches are generally different, $m_{e1} \neq m_{e2}$. The average electron mass is $m_e = (m_{e1} + m_{e2})/2$, the mass difference is $\delta m = (m_{e2} - m_{e1})/2$, and the hole mass is $m_h = m_{h1}$. In the center-of-mass (c.m.) coordinates, the displacement of c.m. motions $\mathbf{R} = (m_e\mathbf{r}_e + m_h\mathbf{r}_h)/(m_e + m_h)$, and of relative motions $\mathbf{r} = \mathbf{r}_e - \mathbf{r}_h$. The exciton c.m. wave vector and relative wave vector are denoted as $\mathbf{Q}$ and $\mathbf{q}$, respectively. We define the exciton mass $M = m_e + m_h$, and the reduced mass $\mu = m_e m_h/M$. The exciton relative motion and c.m. motion are decoupled since $\delta m \ll M$. The Hamiltonian for the bright (dark) excitons $H_{b(d)0} \approx \hbar^2 Q^2/2M_{b(d)} + H_{r,b(d)}$, in which the Hamiltonian of the relative motions is given by $H_{r,b(d)} = \hbar^2 q^2/2\mu_{b(d)} + V(\mathbf{r}) + \Delta_{b(d)}'$. Here the effective mass of bright (dark) excitons is $M_b = M(1 - \delta m/m_e)$ [$M_d = M(1 + \delta m/m_e)$], and the effective reduced mass of bright (dark) excitons $\mu_b = \mu(1 - \delta m/m_e)$ [$\mu_d = \mu(1 + \delta m/m_e)$]. The off-diagonal Rashba term can be rewritten as $H_{BR} = \lambda_{BR}[(m_e/M)\mathbf{Q}_\pm + \mathbf{q}_\pm]$. Due to the large exciton binding energy, the c.m. part of the RSOC (the first term in H_{BR}) can be decoupled from the relative part (the second term). Therefore, we have

$$H_{r,b(d)}\Phi(\mathbf{r}) = E_{b(d)}\Phi(\mathbf{r}), \qquad (4)$$

where $E_{b(d)} = \Delta_{b(d)}' + \varepsilon_{b,b(d)}$ is the ground-state energy of the bright (dark) excitons, and $\varepsilon_{b,b(d)}$ is the exciton binding of bright (dark) excitons in the presence of RSOC (see Appendix A).

The exciton Hamiltonian becomes

$H_{\text{ex},K}$

$$= \begin{bmatrix} \hbar^2|\mathbf{Q}|^2/2M_b - \Delta_{bd}/2 & \lambda_{\text{ex}}^*\mathbf{Q}_- \\ \lambda_{\text{ex}}\mathbf{Q}_+ & \hbar^2|\mathbf{Q}|^2/2M_d + \Delta_{bd}/2 \end{bmatrix} + E_0, \qquad (5)$$

where the energy difference between bright and dark exciton states is

$$\Delta_{bd} \equiv E_d - E_b = -2\lambda_c + \varepsilon_{b,d} - \varepsilon_{b,b}. \qquad (6)$$

We set the zero point of exciton energy $E_0 \equiv (E_b + E_d)/2 = \Delta - \lambda_v + (\varepsilon_{b,d} + \varepsilon_{b,b})/2$, and the RSOC parameters for exci-

tons $\lambda_{\text{ex}} = \lambda e^{i\phi}$, with $\lambda = (m_e/M)|\lambda_{BR}|$, and ϕ is denoted as the gauge phase of RSOC [$\phi = \arg(\lambda_{BR})$]. Similarly, for the K' valley, we have $H_{\text{ex},K'} = H_{\text{ex},K}^*$.

The TMD ML with the finite size could provide a lateral confinement for both the electrons and holes. Without loss of the generality, we consider a circular flake with radius of R_0. In this case, the lateral confinement creates an infinite circular quantum well for exciton c.m. motions, i.e., $H_V = V_0\Theta(R_0 - |\mathbf{r}_{e(h)}|) = V_0\Theta(R_0 - |\mathbf{R} + \frac{m_h}{M}\mathbf{r}|)$. At the lateral boundary $\mathbf{R}_0$, since $\mathbf{R} \gg \mathbf{r}$, the hard wall potential for excitons simplifies to

$$H_V = V_0\Theta(R - R_0), \quad V_0 \to \infty, \qquad (7)$$

which traps the excitons to form the 2D exciton BEC.

Next, we study the dipole-dipole interaction (DDI) between excitons. Under strong external electric field, the electrons and holes are localized on the top and bottom surfaces of the TMD ML, respectively. The DDI can be written as (see Appendix C)

$$V_{dd}(\mathbf{Q}) = \frac{e^2 d}{\epsilon_0 \epsilon}\frac{1 + x_Q\big((\coth\eta_1 + \coth\eta_2) + \frac{1}{2}\big)}{1 + x_Q[\coth(\eta_1 + \eta_2) + 1]}, \qquad (8)$$

where $\eta_{1,2} = \ln[(\epsilon + \epsilon_{1,2})/(\epsilon - \epsilon_{1,2})]/2$, and we take the thin-film limit $|\mathbf{Q}|d \ll 1$. The scattering processes of excitons mediated by DDI, without flipping the exciton spins, are described by

$$H_{dd} \equiv V_{dd}(\mathbf{R}) * (|\psi_b|^2(\mathbf{R}) + |\psi_d|^2(\mathbf{R})), \qquad (9)$$

where the asterisk (symbol $*$) is denoted as the convolution operator.

In addition, we consider the dynamical processes of bright and dark exciton states. The dark A excitons can exist in WSe$_2$ MLs for having long lifetimes ($\tau_d = 59$ ms [44]), and have been experimentally detected [23,45,46]. The bright excitons survive for a few picoseconds. Nonetheless, they can be maintained at a high density by laser pumping, and their lifetimes can be enhanced in the perpendicular electric field. The laser pumping and recombination processes of the bright and dark excitons are included by the pumping and decaying term

$$H_{\text{pd},b} = i\hbar[\hat{R}(\mathbf{R}) - \Gamma_b|\psi_b|^2]$$
$$H_{\text{pd},d} = -i\hbar\Gamma_d|\psi_d|^2, \qquad (10)$$

where $\Gamma_{b(d)} = 1/(2\tau_{b(d)})$. $\tau_{b(d)}$ is the lifetime of bright (dark) excitons.

The bright exciton states can be coupled with the dark states utilizing the magnetic field of the THz laser, known as the electron-spin-resonance technique. The THz field couples the bright and dark states by a Rabi-type term $\hbar\Omega$ in the rotating-wave approximation, accelerating the transition rate between the bright and dark states.

Putting Eqs. (5), (9), (7), and (10) and the off-diagonal THz term together, at low temperatures, the exciton BEC can be well depicted by coupled GP equations

$$i\hbar\frac{\partial}{\partial t}\begin{bmatrix} \psi_b \\ \psi_d \end{bmatrix} = \begin{bmatrix} H_b - \frac{\Delta_{bd}}{2} + H_{\text{pd},b} & -i\lambda e^{-i\phi}\nabla_- + \hbar\Omega \\ -i\lambda e^{i\phi}\nabla_+ + \hbar\Omega & H_d + \frac{\Delta_{bd}}{2} + H_{\text{pd},d} \end{bmatrix}\begin{bmatrix} \psi_b \\ \psi_d \end{bmatrix}, \qquad (11)$$

where the Hamiltonian of the bright (dark) excitons $H_{b(d)} = H_{T,b(d)} + H_V + H_{dd}$. Here the kinetic energy $H_{T,b(d)} = -\hbar^2\nabla_{\mathbf{R}}^2/2M_{b(d)}$.

The exciton BEC at the ground state can be obtained by solving Eq. (11) in the stationary condition. The rate equations for bright and dark states can be constructed from Eq. (11), i.e., $dn_b/dt = \mathcal{R} - \Gamma_b n_b + \mathcal{I}_{bd}$ and $dn_d/dt = -\mathcal{I}_{bd} - \Gamma_d n_d$, respectively. Here we denote the average density of bright (dark) exciton states as $n_{b(d)} = N_{b(d)}/S$ [$N_{b(d)}$ is the number of bright (dark) excitons], the power density of the laser as $\mathcal{R} = \langle\hat{R}\rangle/S$ (in natural unit), and the hopping integral as $\mathcal{I}_{bd} = (-i/\hbar S)\mathrm{Im}[\int \psi_b^* H_{bd}\psi_d dS]$ [H_{bd} is the off-diagonal term in Eq. (11)]. For the stationary state $dn_{b(d)}/dt = 0$, hence, $\mathcal{R} - \Gamma_b n_b = \Gamma_d n_d$. Due to $\Gamma_b \gg \Gamma_d$, we have $n_b \simeq \mathcal{R}/\Gamma_b$. Therefore, the average density of bright exciton states can be tuned by the laser pumping independently. For simplicity, we consider an equal occupation of bright and dark exciton states, i.e., $n_b \simeq n_d$. The more general unequally occupied cases are given in the discussions of the influence of the DDIs. With fixed average density of bright and dark excitons, Eqs. (11) can be reduced to the static coupled GP equations

$$\mu\begin{bmatrix}\psi_b\\\psi_d\end{bmatrix} = \begin{bmatrix}-\frac{\hbar^2\nabla^2}{2M_b} - \frac{\Delta_{bd}}{2} + H_{dd} & -i\lambda e^{-i\phi}\nabla_- + \hbar\Omega\\-i\lambda e^{i\phi}\nabla_+ + \hbar\Omega & -\frac{\hbar^2\nabla^2}{2M_d} + \frac{\Delta_{bd}}{2} + H_{dd}\end{bmatrix}\begin{bmatrix}\psi_b\\\psi_d\end{bmatrix}.$$

(12)

We solve Eqs. (12) with the boundary condition determined by Eq. (7), i.e., $(\psi_b, \psi_d)|_{R=R_0} = 0$, to obtain the ground state of the exciton BEC.

We find that the ground-state excitons can be driven into vortex states in the presence of the gauge field induced by the RSOC. Here we discuss in detail. Equation (5) can be written as $\mathcal{H}_{\mathrm{ex},K} = \gamma^{-1}[\hbar^2(-i\nabla - \mathbf{A})^2/2M] - \gamma[\hbar^2\kappa^2/M] - \sigma_z[\Delta_{bd}/2] + \mathbb{I}[E_0]$ (see Appendix B), where

$$\mathbf{A} = \gamma[-(\kappa_x\sigma_x + \kappa_y\sigma_y)\mathbf{e}_x + (\kappa_y\sigma_x - \kappa_x\sigma_y)\mathbf{e}_y],$$

(13)

$\gamma = \mathbb{I} + \sigma_z[\delta m/m_e]$, and $\kappa_x = \kappa\cos\phi$, $\kappa_y = \kappa\sin\phi$ with $\kappa = \lambda M/\hbar^2$. From this equation, one can see that the RSOC behaves like a SU(2) gauge field acting on the c.m. motion of excitons.

By diagonalizing the Hamiltonian $H_{\mathrm{ex},K}$ [Eq. (5)], we obtain the gapped eigenstates at the K valley

$$\begin{pmatrix}\tilde{\psi}_L\\\tilde{\psi}_H\end{pmatrix} = \begin{pmatrix}\frac{-\beta_+ e^{-i(\theta_Q+\phi)}}{\sqrt{4\lambda^2Q^2+\beta_+^2}} & \frac{2\lambda Q}{\sqrt{4\lambda^2Q^2+\beta_+^2}}\\\frac{-\beta_-}{\sqrt{4\lambda^2Q^2+\beta_-^2}} & \frac{2\lambda Q e^{i(\theta_Q+\phi)}}{\sqrt{4\lambda^2Q^2+\beta_-^2}}\end{pmatrix}\begin{pmatrix}\psi_b\\\psi_d\end{pmatrix},$$

(14)

where $\psi_{b(d)}$ denotes the wave function of bright (dark) excitons without RSOC, and L (H) indicates the lower (higher) exciton state. $\beta_\pm(Q) = \alpha Q^2 + V_\pm(Q)$, $V_\pm(Q) = \Delta_{bd} \pm [(\Delta_{bd} + \alpha Q^2)^2 + 4\lambda^2Q^2]^{1/2}$, where $\alpha \equiv \hbar^2(1/M_d - 1/M_b)/2 \simeq -\hbar^2\delta m/(m_e M)$ arises from the mass difference δm between the bright and dark excitons. While for the K' valley, one can easily obtain the wave function by taking the complex conjugate. The eigenvalues

$$\tilde{H}_{L(H)}(Q) \simeq \hbar^2Q^2/2M + V_\mp(Q)/2 + E_0$$

(15)

at the K/K' valleys are splitted by both the intrinsic SOC and RSOC [Fig. 1(d)].

From Eq. (14), the ground state (L) and the excited state (H) are the hybridization of both the bright and dark exciton

states. Excitons are relaxed to the L state at low temperatures. From Eq. (15), the L-state excitons are trapped in a Mexican-hat-like potential when

$$|\lambda_{\mathrm{BR}}(E_z)| > \hbar\sqrt{\frac{M}{2m_e^2}\left(|\Delta_{bd}| + \frac{\delta m}{m_e}\Delta_{bd}\right)},$$

(16)

compared with the H-state excitons trapped in a steep centrifugal potential in k space. This can be seen clearly by taking the small gap limit $|\Delta_{bd}| \ll 2\lambda Q$, $\tilde{H}_L(Q) \simeq \hbar^2(Q - \kappa)^2/2M + E_0$. That is to say, the ground state of excitons at the L branch is shifted to a finite momentum $\hbar\kappa = \lambda M/\hbar$ [Fig. 1(d)]. This ringlike momentum distribution indicates that the ground-state excitons are no longer static, but can move without dissipation in a superfluid phase. This feature arises from the RSOC since κ is proportional to the strength of RSOC λ.

The Mexican-hat-like dispersion of L-state excitons can further induce the vortices in the BEC regime. The hard-wall potential for bright and dark excitons created by the circular boundary results in the quantization of the wave vector, i.e., $Q_{|\ell_{b(d)}|j} = x_{|\ell_{b(d)}|j}/R_0$, where $x_{|\ell_{b(d)}|j}$ is the jth zero of the Bessel function $J_{|\ell_{b(d)}|}(x)$, and $\ell_{b(d)}$ is the azimuthal quantum number of bright (dark) excitons. The eigenfunctions without RSOC are found to be $\psi_{b(d)}(\mathbf{R}) \propto J_{|\ell_{b(d)}|}(Q_{|\ell_{b(d)}|j}R)e^{i\ell_{b(d)}\vartheta}$. For $Q_{|\ell_{b(d)}|j}R \ll 1$, the $\ell_{b(d)} \neq 0$ solutions

$$\psi_{b(d)}(\mathbf{R}) \propto [\cos\vartheta + i\,\mathrm{sgn}(\ell_{b(d)})\sin\vartheta]^{|\ell_{b(d)}|}R^{|\ell_{b(d)}|}$$

(17)

appear to be vortex states [47]. From Eq. (15) with $Q = Q_{|\ell_{b(d)}|j}$, the ground state of bright (dark) excitons can transit from $\ell_{b(d)} = 0$ to $\ell_{b(d)} \neq 0$, by tuning the strength of the RSOC κ, i.e., the electric fields. When κ exceeds a critical value κ_0, $\tilde{H}_L(Q_{11})$ has lower energy compared with $\tilde{H}_L(Q_{01})$, indicating the rotating status of bright (dark) excitons. For a single vortex $\ell_{b(d)} = 1$, the critical value $\kappa_0 = (Q_{01} + Q_{11})/2 \simeq 3.1183/R_0$. The corresponding critical electric field E_{z0} is determined by

$$|\lambda_{\mathrm{BR}}(E_{z0})| = \frac{\hbar^2}{\sqrt{2}m_e}\sqrt{\kappa_0^2 + \sqrt{\kappa_0^4 + \frac{M^2}{\hbar^4}\Delta_{bd}^2} + \frac{M\delta m\Delta_{bd}}{m_e\hbar^2}},$$

(18)

which restores to Eq. (16) when $\kappa_0 \simeq 0$. As we increase the radius R_0 of the sample (condensate region), the critical electric field decreases due to $E_{z0} \propto 1/R_0$. Equation (18) is a good indicator for the realization of exciton vortices without pumping and decaying. In the condition that bright excitons are tuned by the laser pumping and the bright and dark excitons reach a dynamical equilibrium, we find the electric field required for the vortex creation is reduced, with the numerical results given in the following section.

III. NUMERICAL RESULTS AND DISCUSSIONS

The stationary solution of the Eqs. (12) for fixed numbers of bright and dark excitons, can be solved by the imaginary-time propagation with a normalization step (see Appendix D), which is widely used in ground-state calculations of BEC systems [48–56]. Notice that the final state depends on the choice of initial status. We first consider the states having
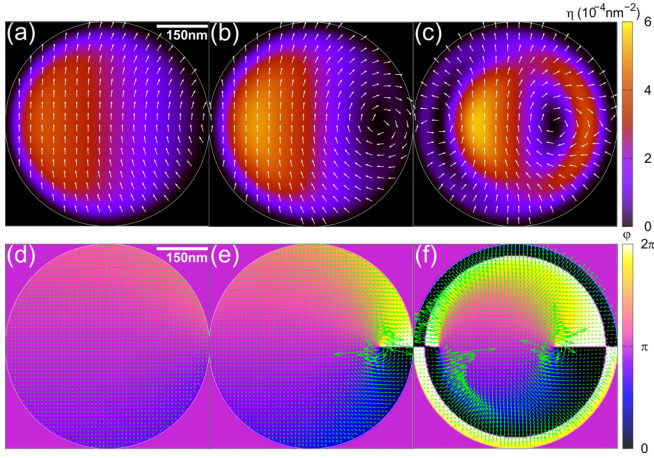
FIG. 2. Motion of a bright exciton vortex at the K valley in a WSe$_2$ flake, varied with perpendicular electric fields. (a)–(c) Show the normalized density $\eta = \rho/N$ (color map) and the unit velocity $\hat{v}$ (white arrows) of the bright excitons at the K valley with fixed average density $n_{b,d} = 10^{10}$ cm^{-2}, at different strengths of the RSOC $|\lambda_{\mathrm{BR}}| =$ (a) 6 meV Å, (b) 12 meV Å, (c) 36 meV Å. (d)–(f) Show the phases φ and the wave vectors $\vec{k} = \nabla\varphi$ (green arrows) corresponding to (a)–(c). The radius of WSe$_2$ flake $R_0 = 0.3$ μm.

zero total orbital angular momentum ($\ell = \ell_b + \ell_d = 0$). In this consideration, although ℓ is conserved, the angular momentum of bright excitons ℓ_b and dark excitons ℓ_d are no longer good quantum numbers. Therefore, pairs of bright and dark exciton vortices can exist.

We take exciton BEC in a circular WSe$_2$ ML flake for instance (other TMD MLs are discussed in the last of this section). The strength of RSOC in the WSe$_2$ ML is $|\lambda_{\mathrm{BR}}| = 0.18E_z$ (eV Å). The electron masses $m_{e1} = 0.29m_0$, $m_{e2} = 0.40m_0$, the hole mass $m_{h1} = 0.36m_0$ (m_0 is the electron rest mass) [43], and the bright-dark splitting $\Delta_{bd} = -37$ meV. We consider the simple free-standing case. The dielectric constants of the substrates (the vacuum) are chosen as $\epsilon_{1,2} = 1.0$, and the WSe$_2$ ML $\epsilon = 4\pi\chi_{2D}/d$, with the 2D polarizability $\chi_{2D} = 7.18$ Å [5]. We also set the gauge phase of RSOC $\phi = \pi/2$ to consist with the normal Rashba form. Hereafter, we choose the average density of bright (dark) excitons $n_{b,d} = 10^{10}$ cm^{-2}, and the radius of the flake $R_0 = 0.3$ μm.

From the numerical calculations of Eqs. (12), we find that the RSOC plays an important role in the ground-state BEC pattern, as shown in Figs. 1(c), 1(e), 2, and 3. The Rashba-induced SU(2) gauge field $\mathbf{A}$ in Eq. (13) arises a spin motive force (SMF) $\mathcal{F} = \hbar^2\kappa^2\sigma_z(\mathbf{Q} \times \hat{\mathbf{z}})/M$, with its direction $\hat{\mathcal{F}}$ determined by the gauge choice of the RSOC, i.e., the phase ϕ. $\mathcal{F}$ would not break the rotational symmetry of the total Hamiltonian [Eq. (12)], but would lead to the separation of the density distribution of the bright and dark states, i.e., the asymmetric pattern of the density distributions shown in Fig. 1(c). More importantly, the RSOC can drive the exciton BEC into a vortex phase. Denoting $\mathbf{Q}_\pm = Qe^{\pm i\theta_Q}$, where $Q = |\mathbf{Q}|$ with $\theta_Q = \arctan(Q_y/Q_x)$, the 2×2 RSOC Hamiltonian composed of off-diagonal terms of $H_{\mathrm{ex},K}$ in Eq. (5) is

$$H_{\mathrm{ex,RSOC}} = \begin{bmatrix} 0 & \lambda e^{-i\phi}Qe^{-i\theta_Q} \\ \lambda e^{i\phi}Qe^{i\theta_Q} & 0 \end{bmatrix}. \quad (19)$$
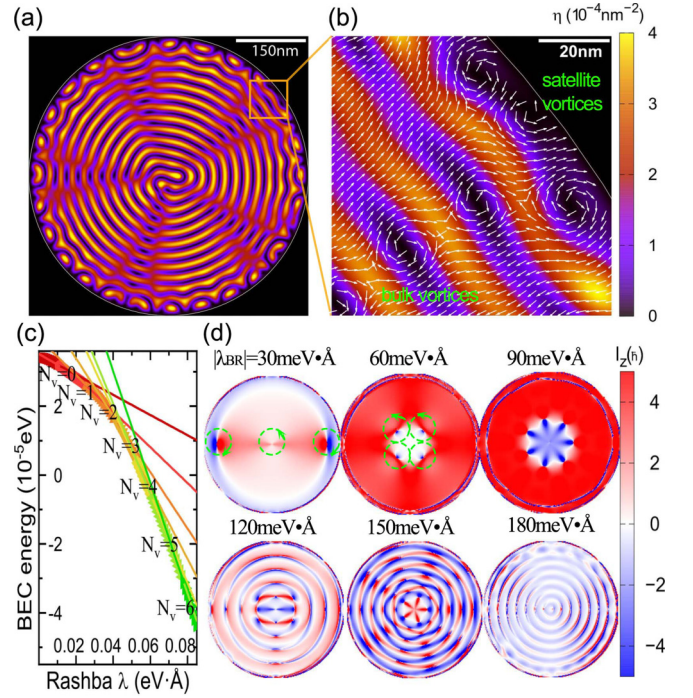

FIG. 3. (a) The normalized density η (color map) and unit velocity $\hat{v}$ (white arrows) distributions of exciton BEC stripe pattern, for the exciton density $n_{b,d} = 1.5 \times 10^{11}$ cm^{-2}, and the strength of RSOC $|\lambda_{\mathrm{BR}}| = 300$ meV Å. (b) The zoom-in of (a) at the edge of the BEC pattern, which shows the satellite vortices at the edge and the bulk vortices located at the radical directions. (c) Phase transitions (indicated by different colors) of bright exciton BEC at the K valley with $\ell = 0$, as a function of the RSOC. N_v is the number of vortices in the sample. (d) The angular momentum distribution l_z (color map) of the ground-state bright vortices for different λ_{BR} in the condition of $\ell \neq 0$, with their positions and directions indicated by green dashed lines and arrows. $n_{b,d} = 1 \times 10^{10}$ cm^{-2} in (c) and (d).

From Eq. (19), the RSOC possesses a phase factor θ_Q in k space, indicating an angular momentum transfer driven by electric fields. The angular phase accumulation of wave functions results in a multivalued solution of ψ_b and ψ_d at a certain point and hence the dislocation of the wavefronts [57], leading to the formation of paired bright-dark exciton vortices [Figs. 1(c)]. Due to the time-reversal symmetry, one can see the mirror-symmetric exciton BEC patterns, i.e., exciton vortices rotating in opposite directions, at the K and K' valleys [Fig. 1(e)]. For simplicity, we focus on the bright exciton vortices at the K valley.

Figure 2 shows the motion of a bright exciton vortex driven by the RSOC induced by perpendicular electric fields. We can see the giant exciton vortex, whose core is indicated by the zero of the wave function $\psi = \sqrt{\rho}e^{i\varphi}$, appears at the boundary and moves to the center as the strength of the RSOC increases [Figs. 2(a)–2(c)]. The diameter of the optically bright vortex can be as large as 200 nm [Fig. 2(b)], which makes it possible to observe experimentally [58,59]. Due to the SMFs $\mathcal{F}$, the density distribution of bright (dark) excitons appears to be a broken ring, containing a vortex. We would like to emphasize that the rotating status of the ground state is revealed by the nonuniform phases of the condensate

wave function as shown in Figs. 2(d)–2(f). The existence of the vortex can be verified by the nontrivial straight-shaped phase jump of φ, along an arbitrary curve around the singular point (the vortex core). The exciton motions in the vortex are illustrated by the velocity distribution $\mathbf{v} = \hbar\mathbf{k}/M$, where $\mathbf{k} = \nabla\varphi$.

As RSOC grows stronger, clockwisely (right half region) and counterclockwisely rotating (left half region) vortices appear simultaneously. The vortices are aligned along the x axis, driven by the increased SMF $\mathcal{F}$ and the DDI-induced repulsion between excitons. The repulsion between the ring fragments also squeezes the vortices into crescent shapes [see Figs. 2(c) and 2(f)]. In Fig. 2(f), we see trivial phase accumulations with cross-shaped phase jumps, which can be eliminated by local phase shifts. Therefore, this type of phase jumps is not related to the presence of the vortices.

Figure 3 shows a variety of exciton vortex states and BEC patterns at the strong RSOC regime. As the RSOC increases, excitons at the edge of the flake roll into rotating satellite vortices [Figs. 3(a) and 3(b)]. The satellite vortices are caused by the interplay of the boundary scattering and the SMF-induced by RSOC. The broken fragments combine together to form ringlike stripes. Compared with line arranged vortices at the small RSOC regime, the vortices [the periodically distributed dark spots in Fig. 3(a)] within the ringlike stripes show different vortex arrangements. This spontaneous symmetry breaking at low temperatures is induced by the Mexican-hat-like dispersion of ground-state excitons in the presence of the RSOC, as we discussed in Sec. II.

The occurrence of the nontrivial phase accumulation could be utilized to define the topology that a jth vortex is topologically protected by a winding number $\mathcal{N}_j$ around the vortex at $\mathbf{x}_j$ [60]:

$$\mathcal{N}_j \equiv \lim_{s_j \to 0} \frac{1}{2\pi} \oint_{\Gamma_{s_j}} \mathbf{k} \cdot d\mathbf{R}, \tag{20}$$

where Γ_{s_j} is a family of closed curves containing $\mathbf{x}_j$ parametrized by s_j. In our calculations (see Appendix E), $\mathcal{N}_j$ are found to be $\mathbb{Z} = \pm 1$, where $+$ $(-)$ corresponds to the vortex rotating clockwisely (counterclockwisely). The total number of vortices can be counted as $N_v = \sum_j |\mathcal{N}_j|$. N_v then actually depicts topologically inequivalent phases.

The phase transitions conserving total angular momentum ($\ell = 0$) can be revealed by the BEC energy [described by Eq. (D5)], which is characterized by different N_v, as shown in Fig. 3(c). The ground-state energies with the number of vortices N_v rely parabolically on the strength of the RSOC λ_{BR} [from Eq. (15), $E_0 \propto -\kappa^2$]. The slope changes suddenly when the system falls into another N_v' state. Therefore, the ground-state phase transitions occur as the RSOC increases.

We further consider the excitons initialized with rotations ($\ell \neq 0$) [61]. By varying ℓ, the global minimum of the BEC energy can be obtained. The excitons may collapse into the ground states having different quantities of bright and dark vortices. To better understand the distribution of vortices with nonzero ℓ, we evaluate the angular momentum $l_z = \hbar\nabla_\vartheta\varphi$, as shown in Fig. 3(d). The vortices at $\mathbf{R} \neq \mathbf{0}$ can be found at the interfaces between positive (red) and negative (blue) l_z branches, while the central vortex at $\mathbf{R} = \mathbf{0}$ is indicated by two
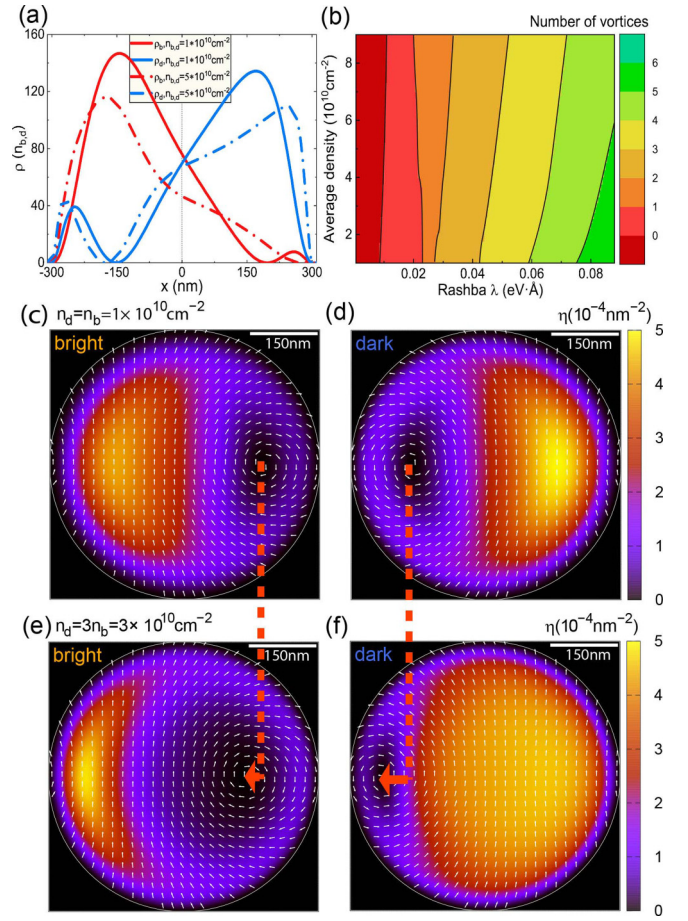

FIG. 4. Impact of exciton densities on the BEC distributions. (a) x-directional profile of exciton densities $\rho = |\psi|^2$ at the K valley. (b) Phase diagram (color map) of the ground state varied with Rashba strength λ_{BR} and average density $n_{b,d}$. (c) The normalized density $\eta = \rho/N$ (color map) and the unit velocity $\vec{e}_\varphi(\hat{v})$ (white arrows) distribution of the bright excitons at the K valley, with equal number of bright and dark excitons. (d) Shows the results of the dark excitons in the same condition of (c). (e), (f) Show the distributions of unequally populated bright and dark excitons, and the relocations of the vortices. The radius of WSe$_2$ flake $R_0 = 0.3$ μm. The strength of the Rashba SOC $|\lambda_{BR}| = 18$ meV Å.

l_z branches of the same signs. With increasing the strength of the RSOC, we find a variety of centrosymmetric BEC patterns, and rearrangements of the bright and dark exciton vortices in Fig. 3(d).

Figure 4 shows the influence of DDI, induced by different densities of bright and dark excitons. Apart from the SMF $\mathcal{F}$ induced by RSOC that separate bright and dark excitons, the repulsive DDI tends to spread the excitons in the BEC region. The strength of the DDI is proportional to the average density of excitons. When the DDI grows stronger, the increasing repulsive interactions separate the excitons in the sample, and push the ring fragments to the edge of the BEC region gradually, as shown in Fig. 4(a). This behavior promotes the formation of satellite vortices. Based on analysis of $\mathcal{N}$ [Eq. (20)], we obtain the relation between the number of vortices N_v and RSOC as well as DDI strength in Fig. 4(b), in the typical $\ell = 0$ condition. Interestingly, we find the N_v

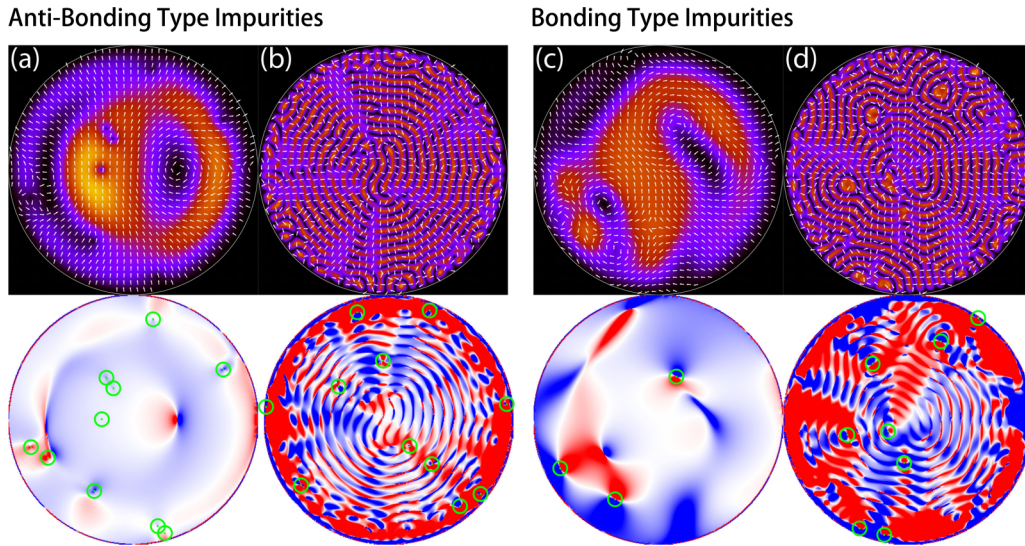Anti-Bonding Type Impurities   Bonding Type Impurities

FIG. 5. The distribution of normalized density η (color map in the first row), velocity unit velocity $\hat{v}$ (white arrows in the first row), and angular momentum l_z (color map in the second row) of bright excitons at the K valley. The influence of random antibonding type impurities on the bulk exciton vortices, and on the satellite vortices, is shown in (a) and (b). While the influence of bonding type impurities are shown (c) and (d), in the same conditions of (a) and (b), respectively. The results are performed at different strengths of the RSOC, $|\lambda_{\mathrm{BR}}|=$ (a) and (c) 36 meV Å, and (b) and (d) 300 meV Å, in a circular flake of WSe$_2$ ML with radius $R_0 = 0.3$ μm. The locations (green circles in the second row) and the total number of the impurities are generated randomly.

phases can be extended to high densities in the relatively weak Rashba SOC regime. We also find the DDI merely affects the vortices in the ring fragments, even if the exciton density is up to several 10^{11} cm^{-2}. We proceed to consider the more general $n_b \neq n_d$ conditions, i.e., $n_d = 3n_b$. We find the exciton vortices contained in the ring fragments almost maintain their positions, while the exciton density distributions are greatly tuned by the DDI, as indicated in Figs. 4(c)–4(f).

The effect of random defects is shown in Fig. 5. Since the samples are relatively large, vacancies, ionic adatoms, and grain boundaries are generally inevitable. Similar to the widely studied pointlike defects created by phase-imprinting techniques in BEC systems [62–64], these types of impurities raise additional local potentials for the condensed excitons. The impurities induced by ionic adatoms led to the local coupling between the conduction and the valence bands, which can be regarded as a term $\tilde{H}'_{cv} = -\lambda_{\mathrm{imp}}$ [65] added to $\tilde{H}_{cv}$ in Eq. (1). The positive (negative) λ_{imp} defines the bonding (antibonding) of the conduction and valence bands. It is reasonable to assume the local impurities as Gaussian trap potentials for both the bright and the dark excitons $V_{\mathrm{imp}}(\mathbf{R}) = \mathcal{A}_{\mathrm{imp}}\exp[-(\mathbf{R}-\mathbf{R}_{\mathrm{imp}})^2/2R_c^2]$, where $V_{\mathrm{imp}}(\mathbf{R}) > 0$ $[V_{\mathrm{imp}}(\mathbf{R}) < 0]$ stands for the antibonding (bonding) type of impurities. Here the radius R_c is comparable to the lattice vector of the TMD MLs. We find that the vortices induced by the RSOC are robust against the antibonding type of impurities [Figs. 5(a) and 5(b)]. In contrast, the bonding type of impurities can destroy the vortices induced by the RSOC, and at the same time create local vortices pinned by the ionic adatoms [Fig. 5(c)]. At the strong RSOC regime, these bound states form new vortex stripes [Fig. 5(d)]. The vacancies (i.e., the selenium monovacancies) introduce tightly localized midgap states [66,67], and hence create deltalike potential traps at

the atomic sites $\mathbf{R}_{\mathrm{imp}}$, i.e., $V_{\mathrm{imp}}(\mathbf{R}) = V_0\Theta(|\mathbf{R} - \mathbf{R}_{\mathrm{imp}}| - R_c)$, capturing the excitons at $|\mathbf{R} - \mathbf{R}_{\mathrm{imp}}| < R_c$. Therefore, the vacancies behave like the bonding type of impurities.

The grain boundaries (also the polycrystalline boundaries) act similarly as the lateral confinement (also the single-crystalline edges) of the ML flake, leading to the significant blueshift of the A-exciton fluorescence [68]. This blueshift greatly increases the exciton energy E_0 of Eq. (5) near the grain boundaries, and hence create potential barriers for the exciton c.m. motions. Compared with the small BEC energy, these potential barriers can be treated as the hard-wall potential boundaries. Hence, the excitons are trapped in an irregularly shaped region, which will lead to the contraction of the BEC patterns and vortices.

We further estimate the critical temperature of the exciton BEC in TMD MLs. The exciton BEC and vortices can be observed even at high temperatures. Although the effective exciton mass in the TMD ML ($\sim 0.71m_0$) is larger than that in semiconductor-coupled quantum wells ($\sim 0.25m_0$) proposed by Butov et $al.$ [69], the average exciton density $n_{b(d)}$ in TMD MLs can be very high. The high exciton density is due to the small Bohr radius of excitons in TMD MLs, which is caused by the enhanced Coulomb interaction in the 2D thin films. This could lead to high critical temperature T_c of the condensation. T_c can be estimated by setting the condensate fraction of the L branch $\xi_L = 1 - \sum_{|m|j}\{\exp\beta_c[\tilde{H}_L(Q_{|m|j}) - \mu] - 1\}^{-1}/nS = 0$ in the weak interacting limit, where $\beta_c = 1/k_BT_c$, $\mu_{T\to 0} = \min(\tilde{H}_L)$, and $S = \pi R_0^2$ is the area of the sample. For example, a WSe$_2$ ML flake with radius of 0.1 μm has $T_c \approx 141$ K, well beyond the temperature zone of liquid nitrogen, when the exciton density is $n_c = 8 \times 10^{12}$ cm^{-2} (the ionization limit given in Ref. [70]). Since the dilute limit of DDI could be applied for

TABLE I. Estimated parameters for excitons in TMD MLs. The exciton c.m. mass M, the reduced mass μ, and the mass difference δm are derived from the band masses $m_{c1,c2,v1}$[43]. m_0 is the free-electron mass. The monolayer thickness d_0 is given by Ref. [43]. The screening length $r_0 = 2\pi \chi_{2D}$ is given by Ref. [5]. The bright-dark splitting Δ_{bd} is derived from the spin splitting in the conduction bands $-2\lambda_c = 2\Delta_{CB}$ [43]. The exciton binding energy is calculated from Eq. (A1), and varies with the applied electric field E_z. The unit of the perpendicular electric E_z is V/Å. The strength of Rashba SOC $|\lambda_{BR}|$ is from Ref. [40].

	MoS$_2$	MoSe$_2$	WS$_2$	WSe$_2$
$\delta m/m_0$	0.015	0.040	0.045	0.055
m_e/m_0	0.455	0.540	0.315	0.345
M/m_0	0.995	1.140	0.675	0.705
μ/m_0	0.247	0.284	0.168	0.176
d_0 (Å)	3.17	3.335	3.14	3.34
r_0 (Å)	41.47	51.71	37.89	45.11
$2\Delta_{CB}$ (meV)	3	20	-31	-37
Δ_{bd} (meV)	-2–3	10–20	-54–-31	-58–-37
λ_{BR} (eVÅ)	$0.033E_z$	$0.055E_z$	$0.13E_z$	$0.18E_z$

$n < n_c$ (see Appendix C), the exciton vortices may survive from the dipolar deviations at finite temperatures.

In the above calculations, we choose WSe$_2$ MLs to illustrate the 2D vortex states of condensed excitons. However, other TMDs can also be used to realize the exciton vortices. Here, we estimate the suitable TMD MLs to realize the exciton vortices experimentally. Equation (16) indicates that smaller bright-dark splitting Δ_{bd} can reduce the RSOC required for the transition into vortex states. Recalling Eq. (6), the bright-dark splitting Δ_{bd} is dependent on binding energy of bright and dark excitons. In TMD MLs, since $\mu_b < \mu_d$, the binding energy of the dark excitons $-\varepsilon_{b,d}$ is larger than the bright excitons $-\varepsilon_{b,b}$, which leads to $\varepsilon_{b,d} - \varepsilon_{b,b} < 0$. The intrinsic spin splitting in molybdenum dichalcogenides (Mo-based) appears to be $\lambda_c < 0$, $\lambda_v > 0$, while in tungsten dichalcogenides (W-based) $\lambda_c > 0$, $\lambda_v > 0$. Hence, the molybdenum dichalcogenides of the TMDs family are predicted to have small Δ_{bd}, as we summarized in Table I. In particular, the MoS$_2$ MLs surrounded by hBN layers (with the dielectric constants $\epsilon_{1,2} = 4.89$ [25]) have vanishing Δ_{bd}. Therefore, the single vortex state can be achieved experimentally in the flakes of MoS$_2$ MLs, under a relatively weak electric field (<1 MV/cm).

Meanwhile, the quantity of exciton vortices is mainly dependent on the strength of the RSOC $|\lambda_{BR}|$, as revealed in Eq. (18). With $|\lambda_{BR}|$ obtained from the DFT calcaulations [40], the tungsten dichalcogenides with heavy chalcogen atoms are good candidates to host the multiple exciton vortices, because of their strong RSOC. Due to the relatively large bright-dark splitting Δ_{bd} in these materials, the applied electric field should be as strong as tens of MV/cm (i.e., utilizing ionically conducting electrolytes [71,72]). We expect WTe$_2$ MLs have more significant vortex structures, but the related data of Te- based TMDs are still lacking. Therefore, we just take WSe$_2$, for example. We believe that the calculations of vortex states in WSe$_2$ are applicable for the family of TMD MLs.

IV. CONCLUSION

In summary, we study the exciton BEC in flakes of TMD MLs in the presence of the RSOC, which couples bright and dark A excitons, and induces ground-state exciton vortices at K and K' valleys rotating oppositely. The clockwise- or counterclockwise-rotating exciton vortex can be created by $\sigma_\pm$ lasers, and protected by the winding numbers. The interplay between the DDI and RSOC leads to the stripe pattern and the phase transitions containing various vortices. The high exciton densities in TMD MLs make it possible to observe the exciton BEC and vortices at higher temperatures. Because of the long lifetime of dark excitons, and the sharp boundary to suppress angular noise raised by pumping, the giant ground-state vortices could sustain long-time evolutions.

APPENDIX A: EXCITON BINDING ENERGY IN THE PRESENCE OF RSOC

Since the TMD MLs are atomically thin, the exciton motions along the z direction are strongly confined. The internal motions of bright and dark excitons containing the RSOC between them can be described by the equation

$$
\begin{bmatrix} -\frac{\hbar^2}{2\mu_b}\nabla^2 + V(\mathbf{r}) & \lambda_{BR}^*(-i\nabla_x - K'\nabla_y) \\ \lambda_{BR}(-i\nabla_x + \nabla_y) & -\frac{\hbar^2}{2\mu_d}\nabla^2 + V(\mathbf{r}) \end{bmatrix} \begin{bmatrix} \Phi_b(\mathbf{r}) \\ \Phi_d(\mathbf{r}) \end{bmatrix}
$$
$$
= \begin{bmatrix} \varepsilon_{b,b} & \\ & \varepsilon_{b,d} \end{bmatrix} \begin{bmatrix} \Phi_b(\mathbf{r}) \\ \Phi_d(\mathbf{r}) \end{bmatrix}. \tag{A1}
$$

We treat the off-diagonal RSOC as perturbation. With the base functions $\Phi_{b0(d0)}(\mathbf{r})$, the unperturbed binding energy $\varepsilon_{b,b0(d0)}$
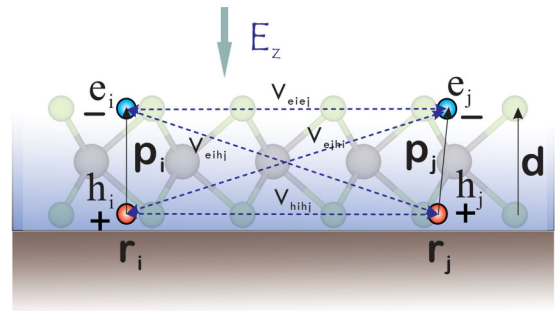

FIG. 6. The schematic dipole-dipole interactions in our system, where V_{eiej} represents the Coulomb interaction between electrons, V_{hihj} between holes, and V_{eihj}, V_{hiej} between electrons and holes. $\mathbf{p}_{i,j}$ are the dipole moments of exciton i and j, and $\mathbf{r}_{i,j}$ are the locations of excitons. $\mathbf{d}$ is the field-induced electron-hole separation.

of the bright (dark) excitons is given by

$$\left[-\frac{\hbar^2}{2\mu_b}\nabla^2 + V(\mathbf{r})\right]\Phi_{b0}(\mathbf{r}) = \varepsilon_{b,b0}\Phi_{b0}(\mathbf{r}),$$

$$\left[-\frac{\hbar^2}{2\mu_d}\nabla^2 + V(\mathbf{r})\right]\Phi_{d0}(\mathbf{r}) = \varepsilon_{b,d0}\Phi_{d0}(\mathbf{r}). \quad \text{(A2)}$$

In polar coordinates, $\Phi_{b0(d0)}(\mathbf{r}) = \frac{1}{\sqrt{2\pi}}e^{im\vartheta}\Phi_{nm}(r)$. With $\int_0^{2\pi} e^{im'\vartheta}e^{i(m+1)\vartheta}d\vartheta = 2\pi\delta_{m',-(m+1)}$, $\Phi_{b(d)}$ and $\varepsilon_{b,b(d)}$ in Eq. (A1) can be obtained by the exact diagonalization of

$$H_r = \begin{bmatrix} \varepsilon_{b,b0} & I_{bd} \\ I_{db} & \varepsilon_{b,d0} \end{bmatrix}, \quad \text{(A3)}$$

where

$$I_{db} \equiv \int \Phi_{d0}^*(\mathbf{r})\lambda_{\text{BR}}(-i\nabla_x + \nabla_y)\Phi_{b0}(\mathbf{r})d\tau$$

$$= \delta_{m'_d,m_b+1}\int_0^\infty \alpha\Phi_{n'_d m'_d}(r)\left(\frac{\partial}{\partial r} - m_b r\right)\Phi_{n_b m_b}(r)r\,dr\,d\vartheta,$$

$$I_{bd} \equiv \int \Phi_{b0}^*(\mathbf{r})\lambda_{\text{BR}}^*(-i\nabla_x - \nabla_y)\Phi_{d0}(\mathbf{r})d\tau$$

$$= \delta_{m_d,m'_b+1}\int_0^\infty \alpha\Phi_{n'_b m'_b}(r)\left(-\frac{\partial}{\partial r} - m_d r\right)\Phi_{n_d m_d}(r)r\,dr\,d\vartheta$$

$$= I_{db}^\dagger. \quad \text{(A4)}$$

In order to calculate Eqs. (A2) and (A3), we use a modified form of Keldysh potential, which takes the spatial separation of electrons and holes $|z_e - z_h| = d$ (d can be evaluated by the thickness of monolayer d_0) into account,

$$V(r) = -\frac{e^2}{4\pi\epsilon_0\rho}\int_0^\infty \frac{e^{-qd}J_0(t)}{(\epsilon_1 + \epsilon_2)/2 + r_0 q}dt, \quad \text{(A5)}$$

where $\epsilon_{1,2}$ are the dielectric constants of substrates, and r_0 is the screening length of the TMD layer [4]. The energy variation induced by the RSOC can also be evaluated by applying Löwdin's perturbation theory to Eq. (A1) in k space, i.e., $\Delta\varepsilon_{b,b} = -\Delta\varepsilon_{b,d} = (1/2\mu_b - 1/2\mu_d)^{-1}\lambda_{\text{BR}}^2/\hbar^2$.

APPENDIX B: GAUGE FIELD INDUCED BY RASHBA SOC

Denoting $\kappa = \lambda M/\hbar^2$, the exciton Hamiltonian (5) in the presence of the RSOC can be written as follows:

$$H_{\text{ex},K} = \frac{\hbar^2}{2M}\begin{pmatrix} \frac{Q_x^2+Q_y^2}{\left(1-\frac{\delta m}{m_e}\right)} & 2\kappa e^{-i\phi}(Q_x - iQ_y) \\ 2e^{i\phi}\kappa(Q_x + iQ_y) & \frac{Q_x^2+Q_y^2}{\left(1+\frac{\delta m}{m_e}\right)} \end{pmatrix} + \begin{pmatrix} -\frac{\Delta_{bd}}{2} & \\ & \frac{\Delta_{bd}}{2} \end{pmatrix} + \begin{pmatrix} E_0 & \\ & E_0 \end{pmatrix}$$

$$\simeq \frac{\hbar^2}{2M}\left[\begin{pmatrix} \left(1+\frac{\delta m}{m_e}\right)Q_x^2 & 2\kappa_x Q_x - 2i\kappa_y Q_x \\ 2\kappa_x Q_x + 2i\kappa_y Q_x & \left(1-\frac{\delta m}{m_e}\right)Q_x^2 \end{pmatrix} + \begin{pmatrix} \left(1+\frac{\delta m}{m_e}\right)Q_y^2 & -2\kappa_y Q_y - 2i\kappa_x Q_y \\ -2\kappa_y Q_y + 2i\kappa_x Q_y & \left(1-\frac{\delta m}{m_e}\right)Q_y^2 \end{pmatrix}\right] - \frac{s_z}{2}\Delta_{bd} + E_0\mathbb{I}$$

$$= \frac{\hbar^2}{2M}\left[\left(\mathbb{I} + \frac{\delta m}{m_e}s_z\right)(Q_x^2 + \kappa^2) + 2(\kappa_x s_x + \kappa_y s_y)Q_x + \left(\mathbb{I} + \frac{\delta m}{m_e}s_z\right)(Q_y^2 + \kappa^2) - 2(\kappa_y s_x - \kappa_x s_y)Q_y\right]$$

$$- \frac{\hbar^2\kappa^2}{M} - \frac{s_z}{2}\Delta_{bd} + E_0\mathbb{I}.$$

When $-2\kappa^2\frac{\delta m}{m_e}s_z \to 0$, we have

$$\hat{H}_{\text{ex},K} = \frac{\hbar^2}{2M}\left(\mathbb{I} + \frac{\delta m}{m_e}s_z\right)(\mathbf{Q} - \mathbf{A})^2 + \frac{\mathbb{I} - s_z}{2}\Delta_{bd} + E_A - \frac{\hbar^2\kappa^2}{M}, \quad \text{(B1)}$$

where the SU(2) gauge field is denoted as

$$\mathbf{A} = \left(\mathbb{I} - \frac{\delta m}{m_e}s_z\right)[-(\kappa_x s_x + \kappa_y s_y)\mathbf{e}_x + (\kappa_y s_x - \kappa_x s_y)\mathbf{e}_y]. \quad \text{(B2)}$$

APPENDIX C: DERIVATION OF DIPOLE-DIPOLE INTERACTIONS

The DDI is composed of four pairs of two-body Coulomb interactions between the charged particles, including (1) two electrons from excitons 1 and 2 [$V_{e1e2}(\mathbf{Q})$], (2) an electron from exciton 1 and a hole from exciton 2 [$V_{e1h2}(\mathbf{Q})$], (3) a hole from exciton 1 and an electron from exciton 2 [$V_{h1e2}(\mathbf{Q})$], and (4) two holes from excitons 1 and 2 [$V_{h1h2}(\mathbf{Q})$]. We set the holes $h1$ at $\mathbf{R}$, $h2$ at $\mathbf{R}'$, and the electrons $e1$ at $\mathbf{R} + \mathbf{p}$, $e2$ at $\mathbf{R}' + \mathbf{p}'$, where $\mathbf{p}$, $\mathbf{p}'$ are denoted as the exciton dipoles. The electrons and holes move in different planes separated by $\mathbf{d}$, under the perpendicular electric field E_z, as sketched in Fig. 6.

By solving the layered Poisson's equations [73,74], we have the Coulomb interactions in k space,

$$V_{e1e2}(\mathbf{Q}) = e^2\left[\left(1 + \frac{\epsilon_1}{\epsilon}\right)e^{Qd} + \left(1 - \frac{\epsilon_1}{\epsilon}\right)e^{-Qd}\right]\Big/\epsilon_0\epsilon_Q Q,$$

$$V_{e1h2}(\mathbf{Q}) = -2e^2/\epsilon_0\epsilon_Q Q = V_{h1e2}(\mathbf{Q}),$$

$$V_{h1h2}(\mathbf{Q}) = e^2\left[\left(1 + \frac{\epsilon_2}{\epsilon}\right)e^{Qd} + \left(1 - \frac{\epsilon_2}{\epsilon}\right)e^{-Qd}\right]\Big/\epsilon_0\epsilon_Q Q. \quad \text{(C1)}$$

Here, the effective dielectric function of the TMD layer is

$$\epsilon_Q = \epsilon\left[\left(1 + \frac{\epsilon_1}{\epsilon}\right)\left(1 + \frac{\epsilon_2}{\epsilon}\right)e^{Qd} - \left(1 - \frac{\epsilon_1}{\epsilon}\right)\left(1 - \frac{\epsilon_2}{\epsilon}\right)e^{-Qd}\right], \tag{C2}$$

and ϵ, $\epsilon_{1,2}$ are the dielectric constants of the TMD ML and substrates.

The DDI can be expressed as

$$V_{dd}(\mathbf{R}, \mathbf{R}', \mathbf{p}, \mathbf{p}') \equiv \int d^2\mathbf{Q}\, e^{i\mathbf{Q}\cdot(\mathbf{R}'-\mathbf{R})} V_{dd}(\mathbf{Q}, \mathbf{p}, \mathbf{p}'), \tag{C3}$$

where

$$V_{dd}(\mathbf{Q}, \mathbf{p}, \mathbf{p}') = V_{e1e2}(\mathbf{Q}) + e^{i\mathbf{Q}\cdot\mathbf{p}'}V_{e1h2}(\mathbf{Q}) + e^{-i\mathbf{Q}\cdot\mathbf{p}}V_{h1e2}(\mathbf{Q}) + e^{i\mathbf{Q}\cdot(\mathbf{p}'-\mathbf{p})}V_{h1h2}(\mathbf{Q}). \tag{C4}$$

Since $\mathbf{Q}$ is an in-plane wave vector, we denote $\mathbf{p}' = \mathbf{d}+\delta\mathbf{p}'$, $\mathbf{p} = \mathbf{d}+\delta\mathbf{p}$. Here the in-plane displacements $\delta\mathbf{p}'(\delta\mathbf{p})$ stand for the deviation of exciton dipoles from the direction of electric field at finite temperatures. As a consequence, the real part of $\exp[i\mathbf{Q}\cdot\delta\mathbf{p}(\delta\mathbf{p}')]$ reduces the two-body Coulomb interactions, while the imaginary part introduces the exponential decay of the interactions varying with the distance between excitons. Both effects cause the decrease of repulsive Coulomb interactions between the charges. Therefore, the strength of DDIs is generally reduced in the presence of the dipole fluctuations.

The dilute limit is applicable at low temperatures, due to the small exciton radius (less than 1 nm), and the average distance between excitons $|\mathbf{R}'-\mathbf{R}| = \sqrt{1/n} \gg |\delta\mathbf{p}'|, |\delta\mathbf{p}|$ (n could be up to several 10^{12} cm^{-2}). The DDI in the dilute limit can be further represented as $V_{dd}(\mathbf{R}, \mathbf{R}') \simeq \int d^2\mathbf{Q}\, e^{i\mathbf{Q}\cdot(\mathbf{R}'-\mathbf{R})}V_{dd}(\mathbf{Q})$, where $V_{dd}(\mathbf{Q}) \equiv V_{dd}(\mathbf{Q}, \mathbf{d}, \mathbf{d})$. We have V_{dd} in reciprocal space

$$V_{dd}(\mathbf{Q}) = \frac{e^2 d}{\epsilon_0\epsilon} \frac{\left(2 + \frac{\epsilon_1+\epsilon_2}{\epsilon}\right)e^{x_Q} + \left(2 - \frac{\epsilon_1+\epsilon_2}{\epsilon}\right)e^{-x_Q} - 4}{x_Q\left[\left(1 + \frac{\epsilon_1}{\epsilon}\right)\left(1 + \frac{\epsilon_2}{\epsilon}\right)e^{x_Q} - \left(1 - \frac{\epsilon_1}{\epsilon}\right)\left(1 - \frac{\epsilon_2}{\epsilon}\right)e^{-x_Q}\right]}, \tag{C5}$$

with $x_Q = Qd$. When $\epsilon > \epsilon_{1,2}$, the Keldysh model is applicable [73], and we obtain Eq. (8).

Since $\lim_{\mathbf{Q}\to 0} V_{dd}(\mathbf{Q}) = \frac{e^2 d}{\epsilon\epsilon_0}$, $V_{dd}(\mathbf{Q})$ is well defined in the momentum space. Therefore, the convolution theorem $\mathcal{F}(H_{dd}) = \mathcal{F}(V_{dd})\mathcal{F}(|\psi_b|^2 + |\psi_d|^2)$ can be safely applied in the DDI calculation of Eq. (9).

APPENDIX D: NUMERICAL ALGORITHM

Introducing length unit r_0 and time unit t_0, setting $r = R/r_0$, $q = Qr_0$, and $E_0 = \hbar/t_0$, we have dimensionless parameters like $V_0 = \delta V/E_0$, $C_{dd} = N\frac{e^2 d}{\epsilon\epsilon_0 r_0^2 E_0}$, $C_q = \frac{\hbar^2}{Mr_0^2 E_0}$, $\lambda_0 = \frac{\lambda}{E_0 r_0}$, $\delta = \frac{\Delta_{bd}}{E_0}$, and $\eta_{1,2} = \frac{1}{2}\ln\frac{\epsilon+\epsilon_{1,2}}{\epsilon-\epsilon_{1,2}}$. From Eqs. (12), the time-independent cGPEs can be written in the dimensionless form as

$$\mu\Psi = \mathcal{F}^{-1}(\mathcal{H}_T\mathcal{F}(\Psi)) + \mathcal{H}_V\Psi, \tag{D1}$$

where the condensate wave function $\Psi = (\psi_b, \psi_d)^T$, the momentum-dependent term $\mathcal{H}_T = \{h_{ij}\}$, $h_{11(22)} = (C_q\eta_{b(d)}q^2 \mp \delta)/2$, $\eta_{b(d)} = 1/(1 \mp \delta m/m_e)$, $h_{21} = h_{12}^* = \lambda_0 e^{i\phi}(q_x + iq_y)$, and potential in real space $\mathcal{H}_V = C_{dd}\mathcal{F}^{-1}[v_{dd}\mathcal{F}(|\psi_b|^2 + |\psi_d|^2)]\mathbb{I}$, with v_{dd} being the dimensionless DDI potential in the paper. We set $\phi = \pi/2$.

For ground-state calculations, we use imaginary-time propagation method, and introduce $\tau = it$ in cGPEs, the Eq. (D1) can be discretized and rewritten as self-aligned iteration through Backward-Euler spectral method (BESP). From τ_n to τ_{n+1}, the imaginary-time cGPEs are given by

$$\mathcal{F}\Psi_{n+1}^* = A[\mathcal{F}\Psi_n - \Delta\tau\mathcal{F}(\mathcal{H}_V\Psi_{n+1}^*)] \tag{D2}$$

followed by a projection step

$$\Psi_{n+1} = \Psi_{n+1}^* / \|\Psi_{n+1}^*\| \tag{D3}$$

to satisfy the normalization condition, where

$$A = [1 + \Delta\tau(\mathcal{H}_T + E)]^{-1}$$
$$= \frac{\begin{pmatrix} 1 + h_{22}\Delta\tau + E\Delta\tau & -h_{12} \\ -h_{21} & 1 + h_{11}\Delta\tau + E\Delta\tau \end{pmatrix}}{(1 + h_{11}\Delta\tau + E\Delta\tau)(1 + h_{22}\Delta\tau + E\Delta\tau) - h_{12}h_{21}} \tag{D4}$$

and E is introduced as a parameter to speed up the convergence, i.e., the energy per particle

$$E(\Psi) = \int E_0 d\mathbf{r}\left[\begin{array}{l} \sum_{j=b,d}\left(\frac{C_q\eta_j}{2}|\nabla\psi_j(\mathbf{r})|^2\right) + |\psi_j(\mathbf{r})|^2\sum_{j'=b,d}\int C_{dd}v_{dd}(|\mathbf{r}-\mathbf{r}'|)|\psi_{j'}(\mathbf{r}')|^2 d\mathbf{r}') \\ -2\lambda_0[\text{Im}(\psi_d^*(\mathbf{r})\nabla_x\psi_b(\mathbf{r})) + \text{Re}(\psi_d^*(\mathbf{r})\nabla_y\psi_b(\mathbf{r}))] + \frac{\delta}{2}(|\psi_b(\mathbf{r})|^2 - |\psi_d(\mathbf{r})|^2) \end{array}\right]. \tag{D5}$$

Note that $\Delta\tau = \tau_{n+1} - \tau_n$. The stopping criterion is for certain tolerance $\forall\, \varepsilon > 0$, $\exists\, N \in \mathbb{N}$ to make $\|\frac{\Psi_n - \Psi_{n+1}}{\Delta\tau}\| < \varepsilon$ for $n \geqslant N$. When the convergence of the energy is more important than that of the wave function, we could also use stopping criterion as $\|\frac{E(\Psi_n) - E(\Psi_{n+1})}{\Delta\tau}\| < \varepsilon_E$.

Since the final state depends on the choice of the initial status, in the presence of local minimums of the BEC energy created by different vortex configurations, we choose the vortex solution

$$\psi_{b(d)}^{\ell} = \frac{1}{\sqrt{\pi}}[x + i\,\text{sgn}(\ell)y]^{|\ell|} \exp\left[-(x^2 + y^2)/a_1^2\right] \tag{D6}$$

as the initial wave function. $N_p = |\ell|$ is the total number of initial vortices and $\ell = 0$ stands for a Gaussian distribution. From our extensive numerical experience, the global minimum of the overall BEC energy can be obtained within our proposal initial data. We also find that the calculated ground-state energy E retains its value as a_1 increases for a particular N_p, while the energy minimum can be reached by setting $N_p = 0, 1$ in the relatively weak RSOC regime.

APPENDIX E: DETECTION OF THE EXCITON VORTICES

For a 2D wave function $\psi(\mathbf{r})$, vortex at $\mathbf{r}_0$ can be detected by the local phase change along an arbitrary close curve Γ around $\mathbf{r}_0$,

$$\kappa(\mathbf{r}_0) = \int_{\Gamma} d\,\arg(\psi) = \int_{\Gamma}[\partial_x \arg(\psi)\,dx + \partial_y \arg(\psi)\,dy] = \int_{\Gamma} d[-i\,\ln(\psi/|\psi|)]. \tag{E1}$$

It is easy to check that $\arg(\psi)$ can be defined continuously, for the continuous wave function ψ locally around $\mathbf{r}_0$, where $\psi(\mathbf{r}_0) \neq 0$ [by picking up a proper branch of $\ln(z)$, $z \in \mathbb{C}$]. For sufficiently smooth ψ (assuming finite number of zeros of ψ), $\kappa(\mathbf{r}_0)$ is a well-defined function for arbitrary $\mathbf{r}_0$ [independent of choices of branches for $\ln(z)$]. For two curves Γ_1, Γ_2, if the area Ω enclosed by Γ_1 and Γ_2 does not contain zeros of ψ, such that $\arg(\psi)$ becomes smooth in Ω, then by Green's formula

$$\int_{\Gamma_2} d\,\arg(\psi) - \int_{\Gamma_1} d\,\arg(\psi) = \int_{\Omega}(\partial_x \partial_y \arg(\psi) - \partial_y \partial_x \arg(\psi))d\mathbf{r} = 0. \tag{E2}$$

This shows that $\kappa(\mathbf{r}_0) = 0$ when $\psi(\mathbf{r}_0) \neq 0$ (as one can shrink the curve Γ_1 to point $\mathbf{r}_0$). When $\psi(\mathbf{r}_0) = 0$, this happens to be the winding number of the possible vortex at $\mathbf{r}_0$, and $\arg(\psi)$ may not be a continuous function locally around $\mathbf{r}_0$ if $\mathbf{r}_0$ is a vortex core. Noticing that $\nabla \arg \psi = \mathbf{v}$ is the velocity [well defined away from vortex or using the definition $\text{Im}(\nabla \psi \bar{\psi})/|\psi|^2$], right-hand side integrand in (2) is the curl of $\mathbf{v}$. Formally, we can calculate the vortex location and winding number by computing curl($\mathbf{v}$).

[1] G. Wang, A. Chernikov, M. M. Glazov, T. F. Heinz, X. Marie, T. Amand, and B. Urbaszek, Rev. Mod. Phys. **90**, 021001 (2018).

[2] K. F. Mak, C. Lee, J. Hone, J. Shan, and T. F. Heinz, Phys. Rev. Lett. **105**, 136805 (2010).

[3] D. Xiao, G.-B. Liu, W. Feng, X. Xu, and W. Yao, Phys. Rev. Lett. **108**, 196802 (2012).

[4] A. Chernikov, T. C. Berkelbach, H. M. Hill, A. Rigosi, Y. Li, O. B. Aslan, D. R. Reichman, M. S. Hybertsen, and T. F. Heinz, Phys. Rev. Lett. **113**, 076802 (2014).

[5] T. C. Berkelbach, M. S. Hybertsen, and D. R. Reichman, Phys. Rev. B **88**, 045318 (2013).

[6] J. Zhou, W.-Y. Shan, W. Yao, and D. Xiao, Phys. Rev. Lett. **115**, 166803 (2015).

[7] K. L. Seyler, P. Rivera, H. Yu, N. P. Wilson, E. L. Ray, D. G. Mandrus, J. Yan, W. Yao, and X. Xu, Nature (London) **567**, 66 (2019).

[8] T. Cao, M. Wu, and S. G. Louie, Phys. Rev. Lett. **120**, 087402 (2018).

[9] H. Yu, Y. Wang, Q. Tong, X. Xu, and W. Yao, Phys. Rev. Lett. **115**, 187002 (2015).

[10] K. F. Mak and J. Shan, Nat. Photonics **10**, 216 (2016).

[11] Q. H. Wang, K. Kalantar-Zadeh, A. Kis, J. N. Coleman, and M. S. Strano, Nat. Nanotechnol. **7**, 699 (2012).

[12] F. Withers, O. Del Pozo-Zamudio, A. Mishchenko, A. P. Rooney, A. Gholinia, K. Watanabe, T. Taniguchi, S. J. Haigh, A. K. Geim, A. I. Tartakovskii, and K. S. Novoselov, Nat. Mater. **14**, 301 (2015).

[13] Y. Cheng, J.-Z. Wang, X.-X. Wei, D. Guo, B. Wu, L.-W. Yu, X.-R. Wang, and Y. Shi, Chin. Phys. Lett. **32**, 117801 (2015).

[14] S. Sun, J. Dang, X. Xie, Y. Yu, L. Yang, S. Xiao, S. Wu, K. Peng, F. Song, Y. Wang, J. Yang, C. Qian, Z. Zuo, and X. Xu, Chin. Phys. Lett. **37**, 087801 (2020).

[15] L. V. Butov, C. W. Lai, A. L. Ivanov, A. C. Gossard, and D. S. Chemla, Nature (London) **417**, 47 (2002).

[16] D. Snoke, S. Denev, Y. Liu, L. Pfeiffer, and K. West, Nature (London) **418**, 754 (2002).

[17] L. V. Butov, A. Zrenner, G. Abstreiter, G. Bohm, and G. Weimann, Phys. Rev. Lett. **73**, 304 (1994).

[18] I. E. Perakis, Nature (London) **417**, 33 (2002).

[19] D. W. Snoke, J. P. Wolfe, and A. Mysyrowicz, Phys. Rev. Lett. **64**, 2543 (1990).

[20] M. M. Ugeda, A. J. Bradley, S.-F. Shi, F. H. da Jornada, Y. Zhang, D. Y. Qiu, W. Ruan, S.-K. Mo, Z. Hussain, Z.-X. Shen, F. Wang, S. G. Louie, and M. F. Crommie, Nat. Mater. **13**, 1091 (2014).

[21] K. He, N. Kumar, L. Zhao, Z. Wang, K. F. Mak, H. Zhao, and J. Shan, Phys. Rev. Lett. **113**, 026803 (2014).

[22] Z. Jiang, Z. Liu, Y. Li, and W. Duan, Phys. Rev. Lett. **118**, 266401 (2017).

[23] Z. Ye, T. Cao, K. O'Brien, H. Zhu, X. Yin, Y. Wang, S. G. Louie, and X. Zhang, Nature (London) **513**, 214 (2014).

[24] J.-H. Choi, P. Cui, H. Lan, and Z. Zhang, Phys. Rev. Lett. **115**, 066403 (2015).

[25] M. M. Fogler, L. V. Butov, and K. S. Novoselov, Nat. Commun. **5**, 4555 (2014).

[26] Z. Wang, D. A. Rhodes, K. Watanabe, T. Taniguchi, J. C. Hone, J. Shan, and K. F. Mak, Nature (London) **574**, 76 (2019).

[27] S. Gupta, A. Kutana, and B. I. Yakobson, Nat. Commun. **11**, 2989 (2020).

[28] F.-C. Wu, F. Xue, and A. H. MacDonald, Phys. Rev. B **92**, 165121 (2015).

[29] O. L. Berman and R. Y. Kezerashvili, Phys. Rev. B **93**, 245410 (2016).

[30] O. L. Berman and R. Y. Kezerashvili, Phys. Rev. B **96**, 094502 (2017).

[31] D. Snoke, Science **298**, 1368 (2002).

[32] D. A. B. Miller, D. S. Chemla, T. C. Damen, A. C. Gossard, W. Wiegmann, T. H. Wood, and C. A. Burrus, Phys. Rev. Lett. **53**, 2173 (1984).

[33] L. V. Butov, A. C. Gossard, and D. S. Chemla, Nature (London) **418**, 751 (2002).

[34] M. A. Can and T. Hakioğlu, Phys. Rev. Lett. **103**, 086404 (2009).

[35] H. Sigurdsson, T. C. H. Liew, O. Kyriienko, and I. A. Shelykh, Phys. Rev. B **89**, 035302 (2014).

[36] H. Dery and Y. Song, Phys. Rev. B **92**, 125431 (2015).

[37] H. Rostami, A. G. Moghaddam, and R. Asgari, Phys. Rev. B **88**, 085440 (2013).

[38] H. Ochoa and R. Roldán, Phys. Rev. B **87**, 245421 (2013).

[39] P. Löwdin, J. Chem. Phys. **19**, 1396 (1951).

[40] A. Kormányos, V. Zólyomi, N. D. Drummond, and G. Burkard, Phys. Rev. X **4**, 011034 (2014).

[41] F. Mahmood, Z. Alpichshev, Y.-H. Lee, J. Kong, and N. Gedik, Nano Lett. **18**, 223 (2018).

[42] Z. Y. Zhu, Y. C. Cheng, and U. Schwingenschlögl, Phys. Rev. B **84**, 153402 (2011).

[43] A. Kormányos, G. Burkard, M. Gmitra, J. Fabian, V. Zólyomi, N. D. Drummond, and V. Fal'ko, 2D Mater. **2**, 022001 (2015).

[44] M. Palummo, M. Bernardi, and J. C. Grossman, Nano Lett. **15**, 2794 (2015).

[45] K.-D. Park, T. Jiang, G. Clark, X. Xu, and M. B. Raschke, Nat. Nanotechnol. **13**, 59 (2018).

[46] S.-Y. Chen, T. Goldstein, T. Taniguchi, K. Watanabe, and J. Yan, Nat. Commun. **9**, 3717 (2018).

[47] K. Y. Bliokh and F. Nori, Phys. Rev. A **86**, 033824 (2012).

[48] K. Góral, K. Rzążewski, and T. Pfau, Phys. Rev. A **61**, 051601(R) (2000).

[49] D. H. J. O'Dell, S. Giovanazzi, and C. Eberlein, Phys. Rev. Lett. **92**, 250401 (2004).

[50] H. Hu, B. Ramachandhran, H. Pu, and X. J. Liu, Phys. Rev. Lett. **108**, 010402 (2012).

[51] Y. Zhang, L. Mao, and C. Zhang, Phys. Rev. Lett. **108**, 035302 (2012).

[52] R. N. Bisset, D. Baillie, and P. B. Blakie, Phys. Rev. A **88**, 043606 (2013).

[53] D. Baillie and P. B. Blakie, New J. Phys. **17**, 033028 (2015).

[54] W. Bao and Y. Cai, SIAM J. Appl. Math. **75**, 492 (2015).

[55] Y. Cai, Y. Yuan, M. Rosenkranz, H. Pu, and W. Bao, Phys. Rev. A **98**, 023610 (2018).

[56] C.-J. Wu, I. Mondragon-Shem, and X.-F. Zhou, Chin. Phys. Lett. **28**, 097102 (2011).

[57] J. F. Nye, M. V. Berry, and F. C. Frank, Proc. R. Soc. London A **336**, 165 (1974).

[58] E. L. Bolda and D. F. Walls, Phys. Rev. Lett. **81**, 5477 (1998).

[59] K. G. Lagoudakis, M. Wouters, M. Richard, A. Baas, I. Carusotto, R. André, L. S. Dang, and B. Deveaud-Plédran, Nat. Phys. **4**, 706 (2008).

[60] M.-A. García-March, A. Ferrando, M. Zacarés, S. Sahu, and D. E. Ceballos-Herrera, Phys. Rev. A **79**, 053820 (2009).

[61] M. Van der Donck and F. M. Peeters, Phys. Rev. B **99**, 115439 (2019).

[62] M. O. Borgh and J. Ruostekoski, Phys. Rev. Lett. **117**, 275302 (2016).

[63] L. J. O'Riordan and T. Busch, Phys. Rev. A **94**, 053603 (2016).

[64] S. G. Rosa, O. Hipólito, and R. Lobo, Phys. Rev. A **11**, 1454 (1975).

[65] Y. Dubi and A. V. Balatsky, Phys. Rev. Lett. **104**, 166802 (2010).

[66] K. Chen, R. Ghosh, X. Meng, A. Roy, J.-S. Kim, F. He, S. C. Mason, X. Xu, J.-F. Lin, D. Akinwande, S. K. Banerjee, and Y. Wang, npj 2D Mater. Appl. **1**, 15 (2017).

[67] V. Carozo, Y. Wang, K. Fujisawa, B. R. Carvalho, A. McCreary, S. Feng, Z. Lin, C. Zhou, N. Perea-López, A. L. Elías, B. Kabius, V. H. Crespi, and M. Terrones, Sci. Adv. **3**, e1602813 (2017).

[68] A. E. Yore, K. K. H. Smithe, W. Crumrine, A. Miller, J. A. Tuck, B. Redd, E. Pop, B. Wang, and A. K. M. Newaz, J. Phys. Chem. C **120**, 24080 (2016).

[69] L. V. Butov, Solid State Commun. **127**, 89 (2003).

[70] A. Chernikov, A. M. van der Zande, H. M. Hill, A. F. Rigosi, A. Velauthapillai, J. Hone, and T. F. Heinz, Phys. Rev. Lett. **115**, 126802 (2015).

[71] K. Prassides, Nat. Nanotechnol. **6**, 400 (2011).

[72] H. Yuan, M. S. Bahramy, K. Morimoto, S. Wu, K. Nomura, B.-J. Yang, H. Shimotani, R. Suzuki, M. Toh, C. Kloc, X. Xu, R. Arita, N. Nagaosa, and Y. Iwasa, Nat. Phys. **9**, 563 (2013).

[73] L. V. Keldysh, Sov. Phys. JETP **29**, 658 (1979).

[74] M. Florian, M. Hartmann, A. Steinhoff, J. Klein, A. W. Holleitner, J. J. Finley, T. O. Wehling, M. Kaniber, and C. Gies, Nano Lett. **18**, 2725 (2018).